Invited Article: Vector and Bragg Magneto-optical Kerr effect for the analysis of nanostructured magnetic arrays

A. Westphalen,[a] M.-S. Lee, A. Remhof, and H. Zabel
Institut für Experimentalphysik/Festkörperphysik, Ruhr-Universität Bochum, 44780 Bochum, Germany

(Received 14 March 2007; accepted 2 September 2007; published online 12 December 2007)

Experimental and theoretical aspects of obtaining the magnetic information carried by laser beams diffracted from an array of micro- or nanosized magnetic objects are reviewed. We report on the fundamentals of vector magneto-optic Kerr effect (MOKE), Bragg-MOKE, and second-order effects in the Kerr signal in longitudinal Kerr geometry as well as on an experimental setup used for vector and Bragg-MOKE experiments. The vector and Bragg-MOKE technique in combination with micromagnetic simulation is a reliable tool for measuring the complete magnetization vector and for characterizing the reversal mechanism of lateral magnetic nanostructures. We discuss the Bragg-MOKE effect for three standard domain configurations during the magnetization reversal process and present the expected behavior of the magnetic hysteresis loops. © *2007 American Institute of Physics.* [DOI: 10.1063/1.2821148]

I. INTRODUCTION

Lateral magnetic nanostructures are of immense scientific and technological interest, since they are used in device applications such as magnetoresistive sensors and high-density and nonvolatile random access memory.[1] There is much interest in the understanding, modeling, and controlling the magnetization reversal of magnetic micro- and nanostructures as a function of shape (stripes, squares, circular dots, elliptic dots, etc.), aspect ratio, and interparticle separation. A review about fabrication and properties of ordered magnetic nanostructures has been provided in Ref. 2. It is well known that in small magnetic structures the shape anisotropy dominates the switching behavior and the switching rate. Therefore the shape and the size of magnetic structures have a strong influence on the switching characteristics.[3–5] In addition, in an array of magnetic elements, interaction and correlation effects between adjacent magnetic structures need to be considered. For the analysis of lateral magnetic nanostructures a number of experimental tools are available: superconducting quantum interference device (SQUID) magnetometry, Hall bars,[6] Lorentz microscopy,[7] x-ray photoelectron emission microscopy (PEEM),[8] magnetic transmission x-ray microscopy (MTXM),[9] magnetic force microscopy,[10] Kerr microscopy,[11] polarized neutron reflectivity (PNR),[12] micro-magneto-optical Kerr effect (MOKE),[13] and MOKE in the diffraction mode (d-MOKE or Bragg-MOKE).[14,15] These methods can be distinguished according to whether they probe magnetic nanostructures locally by imaging techniques (Lorentz microscopy, PEEM, MTXM, Kerr microscopy) or globally by magnetic hysteresis measurements averaging over all elements (SQUID, Hall bars, Bragg-MOKE, PNR).

Particular attention has recently been given to MOKE as a tool to investigate periodic arrays of micron and submicron elements because MOKE is more sensitive to a diminishing amount of magnetic material than SQUID is. If MOKE is operated in the diffraction mode and combined with vector MOKE, information on the magnetization distribution inside of magnetic nanostructures is gained in a vectorial form from remanence to saturation. Furthermore, combining vector-Bragg-MOKE with micromagnetic simulations provides confidence in the proper interpretation of the reversal process. The only limitation is the basic underlying assumption that the magnetization reversal of each nanostructured element is independent and the same and that correlations can be neglected among the elements. If this assumption is not justified, PNR is required for the analysis of fluctuations about the mean magnetization and correlation effects between the different elements.

In this contribution we discuss the vector MOKE (Ref. 16) and the Bragg-MOKE (Ref. 17) technique in the longitudinal geometry, which is highly sensitive to any kind of reversal mechanism. In other studies[15,18] we have shown that the combination of MOKE measurements with micromagnetic simulations for the analysis of the magnetization reversal is a powerful tool for the understanding of the magnetization reversal of lateral magnetic nanostructures. Here we provide a theoretical analysis of the method and discuss the results from simulations of the Bragg-MOKE effect in three standard domain configurations during the reversal process: vortex transition, formation of edge domains, and coherent rotation of the magnetization vector. The aim is to show that Bragg-MOKE is sensitive to these different reversal mechanisms and to provide guidelines for future experimental studies.

The Bragg-MOKE technique is well established in transverse Kerr geometry. In this paper we will show that the advantage of MOKE in the longitudinal Kerr geometry is the possibility to combine vector MOKE with Bragg-MOKE. To overcome the difficulties caused by additional magneto-

[a]Author to whom correspondence should be addressed. Electronic mail: andreas.westphalen@ruhr-uni-bochum.de. URL: www.ep4.ruhr-uni-bochum.de

optical second-order effects of the longitudinal Kerr effect we will discuss a method to separate such nonlinear effects.

This paper is organized as follows: in Sec. II we provide a short overview on the magneto-optical Kerr effect and the experimental setup used for *longitudinal MOKE*. In Sec. III we discuss the *vector* MOKE configuration together with different experimental realizations. Section IV deals with *Bragg* MOKE. Here we first give a short overview on published theoretical and experimental work on the Bragg-MOKE technique, followed by a short description of the experimental setup and a theoretical treatment of the effect. In Sec. V the vector and the Bragg-MOKE signal for some standard nanostructured magnetic arrays are simulated: islands with vortices, stripes with edge domains, and squares with coherent rotation. In Sec. VI second-order magneto-optical effects are discussed. Finally in Sec. VII the theoretical and simulation results are summarized and the advantages of the combination of Bragg and vector MOKE for the analysis of lateral magnetic patterns are discussed.

II. MAGNETO-OPTICAL KERR EFFECT AND EXPERIMENTAL SETUP

When a beam of light is incident from a nonmagnetic medium to a magnetic medium with an arbitrary direction of the magnetization, the dielectric tensor ϵ can be generalized in the first order as follows:[19]

$$\epsilon = \epsilon_{xx}\begin{pmatrix} 1 & -\imath Q m_z & \imath Q m_y \\ \imath Q m_z & 1 & -\imath Q m_x \\ -\imath Q m_y & \imath Q m_x & 1 \end{pmatrix}. \tag{1}$$

All physical quantities are treated as complex numbers. For simplicity, we assume $\epsilon_{zz}=\epsilon_{xx}$. The magneto-optical constant Q is defined as

$$Q = \imath \frac{\epsilon_{xy}}{\epsilon_{xx}}. \tag{2}$$

In Eq. (1), m_x, m_y, and m_z are the direction cosines of the magnetization vector $\mathbf{M}$. Solving Maxwell equations for the above dielectric tensor, the reflected and incident amplitudes E'' and E are related through the Fresnel reflection matrix as

$$\begin{pmatrix} E_s'' \\ E_p'' \end{pmatrix} = \begin{pmatrix} r_{ss} & r_{ps} \\ r_{sp} & r_{pp} \end{pmatrix}\begin{pmatrix} E_s \\ E_p \end{pmatrix}, \tag{3}$$

where r_{ij} is the ratio of the incident i polarized electric field and the reflected j polarized electric field (p stands for p polarization and s for s polarization). MOKE arises because of nonvanishing off-diagonal reflectivity components r_{ps} and r_{sp}. In our case for longitudinal Kerr geometry and an incident s-polarized light beam, the Kerr rotation is expressed by the following reflection coefficients:

$$\theta_K = \Re\left(-\frac{r_{ps}}{r_{ss}}\right), \tag{4}$$

with the general reflection coefficients

$$r_{ss} = \frac{n_1 \cos\alpha - n_2 \cos\alpha'}{n_1 \cos\alpha + n_2 \cos\alpha'} \tag{5}$$

and

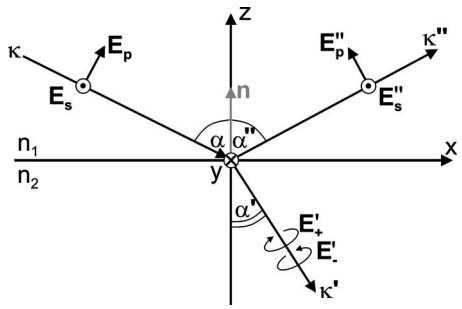

FIG. 1. The coordinate system of the nonmagnetic medium and the magnetic medium with refractive indices n_1 and n_2, respectively. The direction of the magnetization of the magnetic medium is arbitrary.

$$r_{ps} = \frac{\imath n_1 n_2 \cos\alpha (m_x \sin\alpha' - m_z \cos\alpha'')Q}{(n_2 \cos\alpha + n_1 \cos\alpha')(n_1 \cos\alpha + n_2 \cos\alpha')\cos\alpha'}. \tag{6}$$

In the above expressions α, n_1, and n_2 are the angle of incidence, the refractive index of the nonmagnetic medium, and that of the magnetic medium, respectively. The complex refraction angle α' in the magnetic medium is determined by Snell's law, as indicated in Fig. 1. The refracted amplitudes E_+' and E_-' are generally circularly polarized. In longitudinal Kerr geometry, $m_x=1$ and $m_y=m_z=0$. Using Snell's law and simplifying the terms, the Kerr rotation in Eq. (4) can be expressed by[19]

$$\theta_K = \Re\left(-\frac{\cos\alpha \tan\alpha'}{\cos(\alpha-\alpha')}\frac{\imath n_1 n_2 Q}{(n_2^2 - n_1^2)}\right). \tag{7}$$

In Fig. 2 a sketch of a typical setup for longitudinal MOKE measurements is reproduced.[20] A HeNe laser (wavelength $\lambda=632.8$ nm) shines linear polarized light onto the sample under the incident angle α. A Glan-Thompson polarizer ensures the s polarization of the incident light beam, i.e., the light is linear polarized in the direction perpendicular to the plane of incidence spanned by the incoming wave vector κ and the specular reflected wave vector κ''. The sample is mounted with its surface parallel to the field in the center of the pole pieces of the electromagnet on a rotatable sample holder. The sample rotation is controlled by a stepping motor. The electromagnet is a quadrupole magnet. Each pair of the pole pieces can be used independently to generate a magnetic field. The fields of the two pairs intersect perpendicularly at the sample position and reach a maximum magnetic

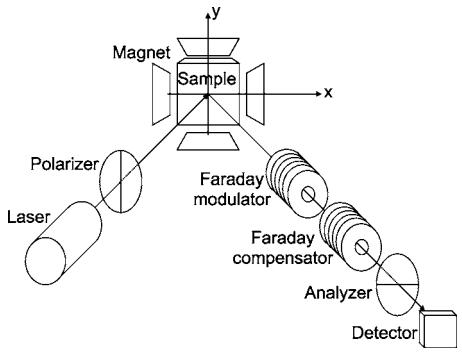

FIG. 2. Schematic of the magneto-optic setup.

field of $H \approx 3000$ Oe. This configuration allows us to set the external magnetic field to any direction parallel to the sample surface without changing the scattering geometry (laser, sample, and detector remain fixed). The magnetic field of each pair of pole pieces is detected by conventional Hall probes. The magnet is mounted together with the sample holder onto a two circle goniometer in the Bragg-Bretano geometry with a fixed detector. The incident angle can be changed from $\alpha_i = 0°$ to 60°. At the sample the light beam is reflected under an angle α'' into the detector unit. In the detector the light passes two Faraday cells called rotator and modulator, an analyzer and finally hits a photodiode. The analyzer, also a Glan-Thompson prism, is crossed with respect to the polarizer. The Faraday cell consists of a glass rod (Schott-Glas, SF 57, diameter $\varnothing = 7.5$ mm, length $l = 80$ mm) surrounded by a coil which produces an axial field in the rod leading to a rotation of the polarization plane according to Verdet's law:

$$\theta_F = VlH_{\mathrm{ax}}, \tag{8}$$

where θ_F is the rotation angle, H_{ax} the axial magnetic field, and V the Verdet constant. One of the two Faraday cells, the modulator, is operated with an ac at a frequency of approximately $\nu = 960$ Hz. Thus, the main polarization plane of the light oscillates with this frequency, which is necessary for the lock-in technique. The other Faraday cell is operated with a dc.

As mentioned before we use a crossed polarizer-analyzer geometry in combination with a Faraday compensator. By means of a lock-in technique, the crossed polarizer-analyzer geometry was achieved at vanishing ν component of the Kerr signal leaving only the 2ν signal caused by the ac itself. The theoretical calculation of the intensity measured by the photodiode is performed using the Jones matrix formalism[21] and leads to the following expression for the intensity function (the compensation induced by the Faraday compensator is assumed to be zero):[22]

$$I = \frac{|r_{ss}|^2}{2}\left[1 + \frac{|r_{ps}|^2}{|r_{ss}|^2} - \left(1 - \frac{|r_{ps}|^2}{|r_{ss}|^2}\right)\cos 2\delta - 2\theta_K \sin 2\delta\right], \tag{9}$$

where $|r_{ss}|$ and $|r_{ps}|$ are the moduli of the corresponding reflection coefficients, and $\delta = \delta_0 \sin(2\pi\nu t)$ is the oscillation of the polarization plane caused by the Faraday modulator. Thus, the detected intensity is proportional to the Kerr rotation angle θ_K. The intensity function in Eq. (9) is plotted in Fig. 3(a). Two frequency components are detected: the double fundamental frequency of the modulation, $2\nu = 1920$ Hz, and a smaller component corresponding to the fundamental frequency $\upsilon = 960$ Hz. For zero Kerr rotation the fundamental frequency will vanish completely. Panels (b) and (c) of Fig. 3 show the power spectrum and the phase of the Fourier transform of the intensity function in (a), calculated using the fast Fourier transformation (FFT) method. In panel (b) two peaks corresponding to the fundamental and the double frequency are visible. The phase information depicted in (c) is important for detecting the sign of the Kerr rotation. This kind of signal is obtained with the phase sensitive lock-in amplifier.

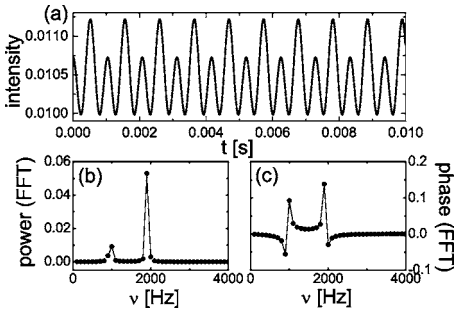

FIG. 3. (a) The intensity function [Eq. (9)] for $\nu = 960$ Hz, $\delta_0 = 2°$, $\theta_F = 0°$, and $\theta_K = -0.25°$. (b) The power spectrum of the signal calculated with FFT, and (c) the phase of the FFT.

Since in our setup we do not use a stabilized laser, we perform the measurement of the Kerr angle θ_K by the compensation method. The Faraday compensator rotates the polarization plane by an angle θ_F in such a way that $\theta_F = -\theta_K$. By measuring the dc of the Faraday compensator, we obtain the Kerr angle θ_K.

III. VECTOR MOKE

In a standard longitudinal MOKE experiment only one component of the in-plane magnetization vector is measured. For the interpretation of the remagnetization process it is advantageous also to measure the orthogonal vector component in order to reconstruct the whole magnetization vector in the sample plane. Using the longitudinal MOKE, a vector magnetometer has been built in the following way.[22,23]

A regular longitudinal MOKE measurement is performed recording the x component of the magnetization vector m_x, i.e., the applied magnetic field lies in the plane of incidence and is orientated parallel to the sample surface. The measured Kerr angle θ_x is proportional to the component of the magnetization vector $\mathbf{M}$ projected into the field direction, $\theta_x \propto m_x$. To determine the complete magnetization vector, a MOKE measurement is performed with the sample and external magnetic field rotated by 90°, such that the angle ϕ between orientation of the sample and field is kept constant, but the magnetization component m_y is in the plane of incidence. In this configuration, where the applied field is in transverse geometry, the Kerr rotation of the longitudinal MOKE detects the magnetization component parallel to the plane of incidence but perpendicular to the applied field, $\theta_y \propto m_y$ (Ref. 23) (see Fig. 4). Both components of the magnetization vector $\mathbf{M}$, m_x and m_y, yield the vector sum of the average magnetization vector $\langle \mathbf{M} \rangle$, as measured within the region illuminated by the laser spot. The illuminated area is approximately 1 mm^2. With χ as the angle between the magnetization vector and external applied field, the magnetization vector can be written as

$$\mathbf{M} = \begin{pmatrix} m_x \\ m_y \end{pmatrix} = |\mathbf{M}| \begin{pmatrix} \cos\chi \\ \sin\chi \end{pmatrix}. \tag{10}$$

Note in Fig. 4 the distinction between the angle χ and the sample angle ϕ, which defines the orientation of the sample with respect to the applied field. Assuming that the proportionality constant between θ_K and the components of $\mathbf{M}$ is

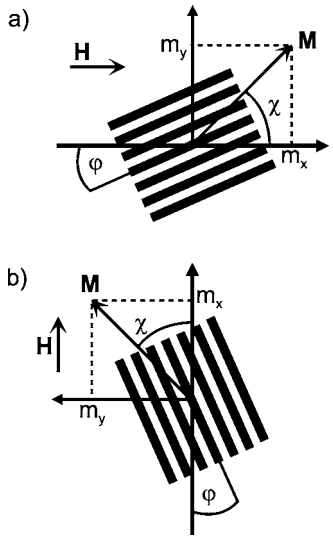

FIG. 4. Definition of the sample rotation ϕ and the angle χ of the magnetization vector **M** for the case of the longitudinal MOKE geometry measuring the component m_x (top panel). In order to measure the component m_y, the external magnetic field and the sample are rotated by 90°, such that the angle ϕ between the structure and the applied field is kept constant, but the magnetization component m_y is in the scattering plane (bottom panel) (Ref. 22).

the same for both configurations, one derives

$$\frac{m_x}{m_y} = \frac{\cos\chi}{\sin\chi} = \frac{\theta_x}{\theta_y}, \tag{11}$$

from which follows the angle of rotation χ of the magnetization vector **M**,

$$\chi = \arctan\frac{\theta_y}{\theta_x}. \tag{12}$$

Furthermore, we can express $M=|\mathbf{M}|$ normalized to the saturation magnetization M_{sat},

$$\frac{M}{M_{\mathrm{sat}}} = \sqrt{\left(\frac{\theta_x}{\theta_{\mathrm{sat}}}\right)^2 + \left(\frac{\theta_y}{\theta_{\mathrm{sat}}}\right)^2}. \tag{13}$$

The distinction between the orientation of the applied field and the component of the magnetization being observed is of key importance for the so-called vector MOKE technique. Both in-plane components of the magnetization vector are measured via the Kerr rotation. Otherwise, using normal longitudinal MOKE for the x component m_x and transverse MOKE for the y component m_y, both components cannot be combined to the whole magnetization vector because of the unknown proportionality between magnetization and Kerr rotation or intensity change, respectively. Assuming linearity, the y component m_y measured in transverse geometry could not be normalized by the saturation field because in the ideal case the sample is fully saturated in the x direction. Thus the magnetization component m_x is 100% and m_y is 0.

To avoid the appearance of both longitudinal and transverse magnetizations in the Kerr signal due to a small misalignment of the polarizer (i.e., not fully s-polarized light) which will complicate the interpretation of the vector MOKE data, the polarizer is carefully aligned until the differences in the hysteresis loop of the y component measured at the specular spot reach nearly zero when the full magnetic field is applied.[24] This polarizer position is also adopted for the measurement of the x component.

As already mentioned, other methods for determining the magnetic vector information from MOKE measurements are described in literature. Ohldag *et al.*[24] extract the vectorial information from longitudinal MOKE measurements by rotating the polarization of the incident light between the measurements, while the orientation of the sample and the applied field remains unchanged. The disadvantage of this method is the lack of quantitative information on the transverse component. Vavassori[25] presents a method for vector magnetometry using a photoelastic modulation technique to obtain m_x, m_y, and m_z. For the component m_y all the optics except the sample are rotated by 45° from the plane of incidence.[26] Florczak and Dahlberg[27] detect the x component of the magnetization vector in the longitudinal geometry and the y component in the transverse geometry. They measured both the intensity shift of the reflected light and the polarization rotation in order to extract both components. An advantage of this method is that sample and magnetic field are kept in fixed positions and the two components can be measured simultaneously. But the two signals are not directly comparable as concerns their magnitude because of the different measured physical quantities.

IV. BRAGG MOKE

A. Literature overview

Bragg-MOKE or diffraction MOKE is a technique where the usual Kerr effect measurements are performed at the diffraction spots from a lateral structure, i.e., the ferromagnetic sample works as a diffraction grating. The first combination of Kerr hysteresis measurements and diffraction from a ferromagnetic grating structure was mentioned by Geoffroy *et al.*.[28] First measurements of MOKE by diffraction were performed by Kranz and Schrödter.[29] They used a homogeneous Fe–Ni thin film and modulated the magnetization distribution in the film, which worked like a diffraction grating. They showed that the first and higher orders of the diffracted light are produced by MOKE whereas the zero order represents the reflectivity of the surface. Experimentally, they determined Kerr intensities versus wavelength, polarization as well as angle of incidence and compared them to those measured by ellipsometric methods. Geoffroy *et al.* measured the transverse Kerr effect at the diffraction spots from an array of micrometer-scale squares of amorphous $Sm_{0.2}Co_{0.8}$. They found that the hysteresis loop measured at the specular reflected spot ($l=0$) was not reproduced in the hysteresis loops obtained from the diffraction spots ($l\neq 0$). The signal in the so-called diffraction hysteresis loops for $l\neq 0$ was not simply proportional to the magnetization like in the specular case and very different results were obtained for different diffraction order l. In order to explain their results Geoffroy *et al.* offered a simple calculation using scalar diffraction theory where two main contributions have to be taken into account. First, the measured intensity involves a geometrical phase shift due to the thickness of the metal film. Second, and that is the important part, the coherent Bragg diffraction spots

carry information on the mean magnetization distribution in the ferromagnetic squares. The intensity change with field for the diffraction spot l is simply related to the variation with the magnetization of the Fourier component of the spatial magnetization distribution within the ferromagnetic squares.

The review article by Grimsditch and Vavassori about Bragg-MOKE in Ref. 14 gives a concise overview on the information in the Kerr signal at the diffraction spots in transverse Kerr geometry. The magneto-optical contribution to the lth order diffracted beam is proportional to the magnetic form factor f_l^m defined by

$$f_l^m = \int_S m(\mathbf{r}) \exp(\imath l \mathbf{G} \cdot \mathbf{r}) dS, \tag{14}$$

where $\mathbf{G}$ is the reciprocal lattice vector, $m(\mathbf{r})$ is the component of the magnetization under investigation, and the integral is carried out over a unit cell of the structure. The measured Kerr signal can be written in the form

$$I \propto \Re(f_l^m) + A_l \Im(f_l^m). \tag{15}$$

In this study A_l has been treated as an adjustable parameter. Unlike the vector MOKE results, the Bragg-MOKE data have no straightforward and easy interpretation. Similar to optical and x-ray diffraction, the lth order diffraction spot represents the lth Fourier component of the magnetic density distribution $m(\mathbf{r})$ in the sample. We have recently extended the Bragg-MOKE method such that vector MOKE can be combined with Bragg-MOKE which allows us to determine the complete magnetization vector data at the lth diffraction spot.[17] This has the advantage that only the periodic part of the MOKE signal is filtered out from all other effects which may contribute to the total MOKE signal.

In the above expression no information on the amplitude of the magnetic signal is provided, only the intensity change is described. Van Labeke *et al.*[30] modeled the amplitude of the magnetic signal as a function of the incidence angle using a perturbation approximation to the Rayleigh method. The theoretical results using the optical constants of the flat surface were in good agreement with their measurements from a diffraction grating obtained in transverse Kerr geometry. Their model also explains the nonexistence of a hysteresis loop for the diffracted order corresponding to a Littrow angle of incidence.[31] An advanced approach for the description of Bragg-MOKE in transverse Kerr geometry is given by Bengoechea *et al.*[32] In their calculations the lateral magnetic structure is described by fluctuations in the dielectric tensor. The latter approach can also be used to describe the longitudinal Bragg-MOKE.

A number of experimental and theoretical publications followed after the seminal report by Geoffroy *et al.*[28] In the following some of these studies are briefly discussed.

- Bardou *et al.*[33] studied the interplay between diffraction and magneto-optics by measuring the Kerr rotation from Co dots (diameter of $1-2$ μm) in polar Kerr geometry. The Kerr rotation shows strong variations versus the diffraction order, the light polarization direction, and the ratio of the film to background reflectance.
- Souche *et al.*[34] performed Bragg-MOKE in transverse Kerr geometry on a commercial ferromagnetic grating presenting systematic measurements of the change in reflectivity between oppositely saturated magnetic states, and for various diffracted beams by varying the angle of incidence.
- Eremenko *et al.*[35] observed that under experimental conditions the magnitude of the transverse Kerr effect measured in diffracted beams on an array of Fe_3Si stripes (width of 0.5 μm, period of 3.5 μm) is much greater than the maximum value for a sample with a flat surface. They assumed that the enhancement of the TMOKE by an array of magnetic stripes is due to the cancellation between the light interacting with the surface of the magnetic stripes and the light interacting with the nonmagnetic substrate.
- Gadetsky *et al.*[36] measured Kerr loops in the diffracted beams on deep grooved glass substrates with amorphous TbFeCo (groove depth of 50–400 nm, period of 1 μm) showing constructive and destructive interferences of the beams reflected from grooves and lands as a function of the effective phase depths and relative widths of grooves and lands.
- Vavassori[25] investigated the magnetic properties of a dot array that contains two nonidentical dots per unit cell (thickness of 40 nm, ellipses with 0.4 and 0.7 μm axes, circular dots of 0.4 μm in diameter). This structure produces a diffraction pattern consisting of intense and weak spots that results from in- and out-of-phase contributions of the two sublattices. A comparison of the magneto-optical Kerr measurements on the weak and strong diffraction spots enables the switching of the two sublattices to be determined independently. In a further study[37] they investigated the magnetic properties of an array of holes in an Fe film (thickness of 40 nm, diameter of 200 nm, period of 2 μm). They developed a theory of diffraction from an array to include magneto-optic effects. The theory allows us to interpret the differences in the magnetic loops observed on the reflected beam and those observed on diffracted spots. The latter contain more detailed information on the magnetic structure in the vicinity of the holes and allow to infer differences in the switching mechanism for fields applied along the easy and hard axes.
- Guedes *et al.*[38] studied the reversal mechanism for the magnetization in an Fe film with an array of elliptical holes as a function of temperature and the angle between the applied magnetic field and an ellipse axis. Transverse and longitudinal magnetization components and minor magnetization loops are explored in order to understand the reversal process. The experimental results are interpreted using micromagnetic simulations. The simulations account for the strong angular dependence of the hysteresis loops and provide a detailed picture of how the local magnetization evolves during reversal.
- For the Bragg-MOKE technique it is not necessary to have a structurally patterned sample. Also a homogeneous film with a regular magnetic pattern sample will show diffraction spots where hysteresis loops can be measured. Costa-Krämer *et al.*[39] report on magneto-optic diffraction by a periodic domain structure generated in a flat ferromagnetic metal by coupling it magnetically to an array of magnetic

elements. Both exchange and magnetostatic coupling are effective, creating a modulation of the magnetization. Micromagnetic simulations agree qualitatively with their experimental results.

- In Ref. 40 Suzuki *et al.* present a theory for the magneto-optical effect in an array of magnetic dots for normal incidence, in the limit of large lattice spacings and negligible edge effects. Their calculations predict (i) that in the diffraction order of polar angle α, the ratio of the complex Kerr rotations for *s* and *p* incident polarizations is equal to $\cos^2 \alpha$ and (ii) that the relative area occupied by the magnetic dots can induce a resonance of the Kerr rotation at specular reflection.
- Wenzel *et al.*[41] present explicit expressions for magneto-optic interference and diffraction effects which can be applied to arbitrary thin-film systems and to arbitrary magnetization patterns.
- The light diffracted by the spacing between the stripes will also contribute to the Bragg-MOKE signal. In Ref. 42 Schmitte *et al.* studied the interference between light diffracted by the not ferromagnetic substrate and a ferromagnetic Ni stripe array. The interference leads to a modification of the observed Kerr rotation much in the same way as antireflection coatings on thin films help to increase the magneto-optical contrast in Kerr microscopy.
- In Ref. 18 the authors investigated the magnetization reversal of a spin-valve structure: Co stripes on Fe(001). The results show an enhanced Kerr rotation in the spin-valve regime. This behavior is due to an increasing amplitude of the light diffracted by the Co grating compared to the Fe grating. Furthermore, hysteresis of odd and even orders of diffraction is significantly different, which can be understood on the basis of the existence of edge domains.
- The investigation of a complex domain structure with vector and Bragg-MOKE is reported in Refs. 15 and 43. The authors studied the remagnetization process of triangular Fe rings. Triangular structures have a sixfold magnetic shape anisotropy. The geometry of this structure leads to more possibilities of the remagnetization process according to the orientation of the structure to the applied magnetic field. It is possible to tailor the remagnetization process by changing the size of the triangular rings or by introducing asymmetries. The vector and Bragg-MOKE results agree with micromagnetic simulations and magnetic force microscopy images.

Further examples where the Bragg-MOKE technique is used for the investigation of the remagnetization process can be found in Refs. 44 and 45 (square and elliptical holes in an Fe film), Ref. 46 (an array of Permalloy dots), Refs. 47 and 48 (Fe stripes), and Ref. 49 (Co microsquare array).

This list of references shows that the Bragg-MOKE technique is widely used for the investigation of the remagnetization process in lateral magnetic structures. Bragg-MOKE can easily be performed. In principle, it is possible with any standard MOKE setup as long as the diffraction spots from the lateral structure can be guided into the detector.

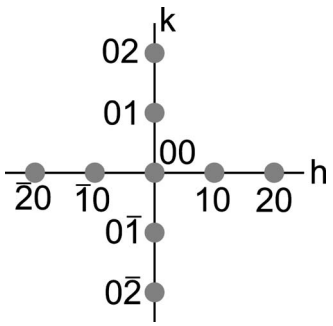

FIG. 5. Sketch of the diffraction pattern and nomenclature of the diffracted beams. Intermediate diffracted beams are not taken into account.

B. Experimental setup

Bragg-MOKE is measured like for most common diffraction experiments in the Fraunhofer diffraction geometry. The laser, the sample, and the magnet are mounted on a goniometer such that the angle of the incident beam and the reflected beam can be varied between −60° and 60° with respect to the surface normal. For the Bragg-MOKE study the angle of incidence is usually set to $\alpha=0°$ (perpendicular incidence) ensuring a symmetrical diffraction pattern. The structured sample is orientated with the normal of the surface in the plane of incidence and with the external magnetic field parallel to the surface. The Kerr effect is measured in the longitudinal configuration with *s*-polarized light. In the next paragraph a theoretical expression of the Bragg-MOKE in longitudinal Kerr geometry is given. To distinguish between diffracted beams lying in the plane of incidence and the ones perpendicular to that plane, we label the in-plane diffracted beams with $h0$, the out-of-plane ones $0k$ (see Fig. 5). The combined hk diffracted beams are not considered here.

C. Theoretical treatment

An exact expression for the electric field vector at point *P* far removed from the surface *S* of a grating illuminated by an incident plane wave is given by the Stratton-Silver-Chu integral[50]

$$\mathbf{E}(P) = A\kappa'' \times \int_S \left[\mathbf{n} \times \mathbf{E}' - \frac{n_2}{\sqrt{\mu'}} \kappa'' \times (\mathbf{n} \times \mathbf{H}') \right] \times \exp[\imath k(\kappa'' - \kappa) \cdot \mathbf{r}] dS, \tag{16}$$

where κ and κ'' are unit vectors in the direction of propagation of the incident and scattered waves, respectively, and $\mathbf{E}'$ and $\mathbf{H}'$ are the electric and magnetic field vectors at point $\mathbf{r}$ on the surface where the local normal is $\mathbf{n}$. Finally, $k=2\pi/\lambda$ and $A=\imath k \exp(\imath k R_0)/(4\pi R_0)$, μ' and n_2 are the permeability and refractive index of the immersion medium, respectively, and R_0 is the distance from the origin to the field point *P*. The physical-optics approximation assumes that the $\mathbf{E}$ and $\mathbf{H}$ fields at any point on the surface *S* are the same as they would be if that point were part of an infinite tangent plane. Therefore the Fresnel reflection formulas are assumed to hold locally at each point with the angle of incidence taken to be that between the incident wave vector and the normal one.[50]

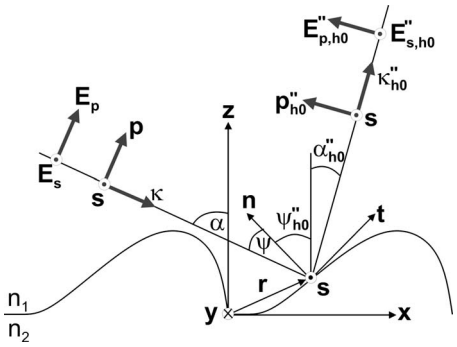

FIG. 6. Definitions of the various directions and angles mentioned in the text.

In the following, it is assumed that the diffraction is caused by a groove grating, i.e., only the diffraction in the plane of incidence is taken into account. This simplifies the problem considerably. In principle, the approach in Eq. (16) can be used for explaining the Bragg-MOKE signal at diffraction spots outside the plane of incidence. But this is not an exact solution of the problem of scattering of light of p and s polarizations by a diffraction grating as we use the physical-optics approximation. We will show that there is agreement between some features of the theory and experiment. Our aim is not to calculate exact magnitudes but to show the origin of the measured Bragg-MOKE signals in longitudinal Kerr geometry. Therefore, we will later on treat for our samples unknown coefficients as adjustable parameters to keep the problem simple.

In Fig. 6 the directions and angles are defined. (x,y,z) is a right-handed Cartesian coordinate system with x running parallel to the grooves and z normal to the mean surface level. $(\mathbf{s},\mathbf{t},\mathbf{n})$ is a right-handed mutually orthogonal set of unit vectors defined at each point with position vector $\mathbf{r}$ on the surface of the grating where $\mathbf{s}$ and $\mathbf{t}$ are parallel to the rulings and tangent to the groove profile, respectively, and $\mathbf{n}=\mathbf{s}\times\mathbf{t}$ is the local unit normal. κ and κ''_{h0} are unit vectors in the direction of the propagation of the incident and hth diffracted waves, respectively. α and α''_{h0} are the angle of incidence and the angle of diffraction of the hth order, respectively, and ψ is the local angle of incidence. The directions of polarizations $\mathbf{s}$, $\mathbf{p}$, and $\mathbf{p}''_{h0}$ follow the usual conventions. At the interface the normal components of $\mathbf{D}$ and $\mathbf{B}$ as well as the tangential components of $\mathbf{E}$ and $\mathbf{H}$ are continuous. Since $\mathbf{B}=\mu\mathbf{H}=n\sqrt{\mu}(\kappa\times\mathbf{E})$ and $\mathbf{D}=\epsilon\mathbf{E}$, these relations lead to the following conditions at the interface:

$$[\epsilon(\mathbf{E}+\mathbf{E}'')-\epsilon'\mathbf{E}']\cdot\mathbf{n}=0, \tag{17}$$

$$[n_1\sqrt{\mu}(\kappa\times\mathbf{E}+\kappa''\times\mathbf{E}'')-n_2\sqrt{\mu'}(\kappa'\times\mathbf{E}')]\cdot\mathbf{n}=0, \tag{18}$$

$$(\mathbf{E}+\mathbf{E}''-\mathbf{E}')\times\mathbf{n}=0, \tag{19}$$

$$\left[\frac{n_1}{\sqrt{\mu}}(\kappa\times\mathbf{E}+\kappa''\times\mathbf{E}'')-\frac{n_2}{\sqrt{\mu'}}(\kappa'\times\mathbf{E}')\right]\times\mathbf{n}=0, \tag{20}$$

where $\mathbf{n}$ is the normal vector, ϵ the dielectric tensor, and the permeability for the alternating magnetic field of the light wave is set to 1, $\mu=\mu'=1$ (this is a reasonable approximation in the visible range of light). After simple vector-algebraic manipulations the quantities in the integrand of Eq. (16), involving the field vectors, the relations of Eqs. (17)–(20), and the electric field vectors as defined in Fig. 6, become for the p polarization and s polarization, respectively:

$$\mathbf{n}\times\mathbf{E}'=\mathbf{s}E_p[r_{pp}\cos(\alpha''_{h0}+\psi''_{h0})-\cos\psi]+\mathbf{t}E_p r_{sp}, \tag{21}$$

$$\frac{n_2}{\sqrt{\mu'}}\mathbf{n}\times\mathbf{H}'=-\mathbf{s}E_p r_{sp}\cos(\alpha''_{h0}+\psi''_{h0})+\mathbf{t}E_p(r_{pp}+1), \tag{22}$$

$$\mathbf{n}\times\mathbf{E}'=\mathbf{s}E_s r_{ps}\cos(\alpha''_{h0}+\psi''_{h0})+\mathbf{t}E_s(r_{ss}+1), \tag{23}$$

$$\frac{n_2}{\sqrt{\mu'}}\mathbf{n}\times\mathbf{H}'=-\mathbf{s}E_s[r_{ss}\cos(\alpha''_{h0}+\psi''_{h0})-\cos\psi]+\mathbf{t}E_s r_{ps}. \tag{24}$$

Here E_p and E_s are the field amplitudes of the incident wave of the respective polarizations, and r_{ij} are the local Fresnel reflection coefficients. Carrying out the various vector multiplications involved, the electric fields of the hth order for both polarizations can be written as

$$\mathbf{E}''_{s,h0}=-AE_s\int_S\{\mathbf{s}[\cos(\alpha''_{h0}+\psi''_{h0})(2r_{ss}+1)-\cos\psi]+\mathbf{p}''_{h0}[2r_{ps}\cos(\alpha''_{h0}+\psi''_{h0})]\}\exp[\imath k(\kappa''_{h0}-\kappa)\cdot\mathbf{r}], \tag{25}$$

$$\mathbf{E}''_{p,h0}=-AE_p\int_S\{\mathbf{p}''_{h0}[\cos(\alpha''_{h0}+\psi''_{h0})(2r_{pp}+1)-\cos\psi]+\mathbf{s}[2r_{sp}\cos(\alpha''_{h0}+\psi''_{h0})]\}\exp[\imath k(\kappa''_{h0}-\kappa)\cdot\mathbf{r}]. \tag{26}$$

The scattered electric field is pointing along the directions predicted by the grating equation

$$\sin\alpha''_{h0}=\sin\alpha-\frac{h\lambda}{d}, \tag{27}$$

with $h=0,\pm1\pm2,\ldots$, the grating period d, and the incident laser beam wavelength λ. In the Bragg-MOKE measurements the incident laser beam is s polarized, i.e., $E_p=0$. Thus, only Eq. (25) has to be taken into account. This equation already shows that the incident linear s polarization is changed into a polarization containing s and p components after reflection. This is due to the reflection coefficient r_{ps} which is proportional to the magneto-optical constant Q and, finally, to the magnetization. For simplicity, the terms of the integrand are abbreviated as

$$\mathbf{E}''_{s,h0}=-AE_s(\mathbf{s}E''_{ss,h0}+\mathbf{p}''_{h0}E''_{ps,h0}). \tag{28}$$

The term $E''_{ss,h0}$ only depends on the reflection coefficient r_{ss}, and the term $E''_{ps,h0}$ contains only the reflection coefficient r_{ps}. In a linear approximation as considered in this case, the reflection coefficient r_{ss} is not affected by the magnetization.[51] Thus, Eq. (25) can be split into a nonmagnetic part

and a magnetic part. In the MOKE setup described above the diffracted laser beam passes a Faraday modulator and an analyzer, which is in crossed position to the incident *s*-polarized light, before it hits a photodiode. The Faraday modulator leads to an oscillation of the polarization plane, with an oscillation angle $\delta=\delta_0 \sin(2\pi\nu t)$ as described in Sec. II. The electric field E_d at the photodiode is

$$E_d = (E''_{ss,h0} \sin\delta + E''_{ps,h0} \cos\delta). \tag{29}$$

The detecting photodiode measures the intensity of the light beam after the analyzer, $I=|E_d|^2$. $E''_{ss,h0}$ corresponds to the nonmagnetic part and $E''_{ps,h0}$ to the magnetic part. Since the amplitude of the oscillation is $\delta_0 \approx 2°$, the term with $E''_{ps,h0}$ dominates. The integral

$$E''_{ps,h0} = \int_S [2r_{ps} \cos(\alpha''_{h0} + \psi''_{h0})] \exp[\imath k(\kappa''_{h0} - \kappa)\cdot \mathbf{r}] dS \tag{30}$$

corresponds to the magnetic form factor in Eq. (14). The information about the magnetization is given by the reflection coefficient r_{ps}. In our case of a rectangular shape profile, the term with $\alpha''_{h0}+\psi''_{h0}$ is constant at the surface of the magnetic structure and can be taken in front of the integral. Therefore the measured intensity can be expressed by Eq. (15) like in the case of the transverse Kerr geometry.[14] The same formalism which explains the Kerr signal measured at the diffraction spots in transverse Kerr geometry in Ref. 46 can also be used in longitudinal Kerr geometry. The present approach starting from the Stratton-Silver-Chu integral in Eq. (16) has the advantage that it takes into account arbitrary shapes of the lateral structure, the differences in height leading to a geometrical phase shift, and the effects according to different materials at the surface of the lateral structure, e.g., if ferromagnetic Fe elements are set on top of a homogeneous Co film as in Ref. 18.

The Bragg-MOKE technique, which is well established in transverse Kerr geometry, is not restricted to this geometry. The Bragg-MOKE measurements in the longitudinal geometry are equivalent to those in the transverse geometry and can be interpreted with the same formalism. It is up to the choice of the experimenter which Kerr geometry is used. One advantage of the longitudinal geometry is the possibility to combine vector MOKE with Bragg-MOKE without changing the measurement geometry. As the absolute Kerr rotation and not the relative intensity change is measured, the longitudinal Kerr effect can be used for vector magnetometry where the results of the both vector components can be compared qualitatively and quantitatively. There are also disadvantages using the longitudinal Kerr effect, for example, additional second-order effects may complicate the interpretation of the observed hysteresis loops. On the other hand, nonlinear magneto-optic effects can easily be corrected, as shown in Sec. VI.

The use of off-specular diffracted beams for magneto-optical measurements has also some technical advantages. The Kerr amplitude in saturation can be increased by choosing high order of diffraction, but this gain is paid by a strong decrease in intensity. Bragg-MOKE acts like a filter because only signals from the grating can pass. On the other hand light diffracted by the spacing between the grating elements also contributes to the total signal. The interference between light diffracted by the nonferromagnetic substrate and the ferromagnetic structure elements may lead to modifications of the observed Kerr signal.

Finally, it is possible to combine Bragg-MOKE with vector MOKE measurements at higher order diffraction spots. In Sec. III vector MOKE has been introduced for measurements at the specular reflected spot. If sample and field are orientated for a vector MOKE measurement of the *x* component, the Kerr signal measured at the diffraction spots will reflect the magnetic form factors of the magnetization component m_x,

$$f^{m(x)}_{hk} = \int_S m_x(\mathbf{r}) \exp(\imath \mathbf{G}_{hk}\cdot\mathbf{r}) dS, \tag{31}$$

where $\mathbf{G}_{hk}\cdot\mathbf{r}=hx/d_x+ky/d_y$, x and y are the components of the vector $\mathbf{r}$, d_x and d_y are the periodicities of the lateral structure parallel and perpendicular to the plane of incidence, and h and k are the diffraction orders of the beams lying in the plane of incidence and perpendicular to the plane, respectively. In the second case where sample and field are orientated for a vector MOKE measurement of the *y* component, the measured signal at the spots will reflect the magnetic form factors of the magnetization component m_y,

$$f^{m(y)}_{hk} = \int_S m_y(\mathbf{r}) \exp(\imath \mathbf{G}_{hk}\cdot\mathbf{r}) dS. \tag{32}$$

The combination of both techniques provides a wealth of information about the remagnetization process and gives a much deeper insight than a standard longitudinal Kerr hysteresis measurement alone. Form factors obtained from diffraction spots lying in the scattering plane, f^m_{h0}, are different from form factors from diffraction spots perpendicular to the scattering plane, f^m_{0k}. In principle it is possible to obtain the two form factors f^m_{h0} and f^m_{0k} simultaneously using two detectors. For example, if sample and field are orientated for the case that the magnetization component m_x is measured, then from the higher order diffraction spots lying in the scattering plane the form factor $f^{m(x)}_{h0}$ is obtained and the form factor $f^{m(x)}_{0k}$ will be measured at the higher order diffraction spots perpendicular to the scattering plane. Rotating sample and field by 90° allows to measure the form factors for the magnetization component m_y.

V. BRAGG-MOKE SIMULATIONS

In this section the Bragg-MOKE effect for some standard configurations is simulated. As pointed out above the hysteresis measurement at the *l*th order of diffraction corresponds to the *l*th Fourier component of the magnetization distribution ($l=h,k$). In the following the real and imaginary parts of the magnetic form factor calculated using Eqs. (31) and (32) are presented as a function of the magnetic field for some cases of present interest.

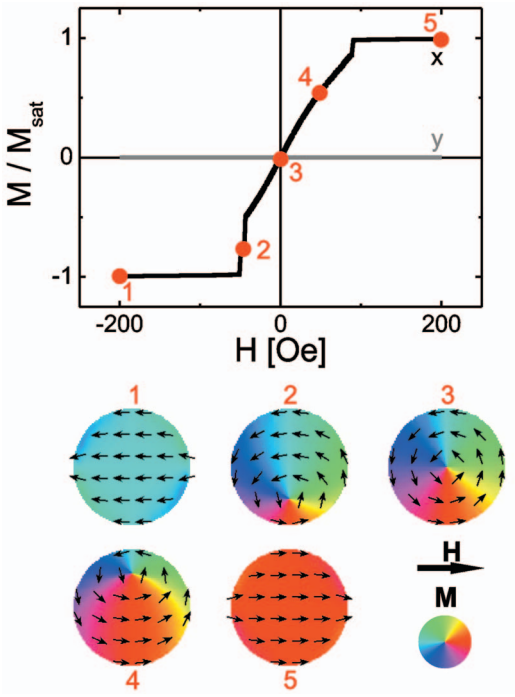

FIG. 7. (Color) Ascending branch of the hysteresis loop for the x (black line) and the y component (gray line) of the magnetization, and some selected calculated magnetization profiles.

A. Circular islands with vortex state

Here we consider a model for the remagnetization process of circular dots via a vortex state at remanence. In the micromagnetic simulation performed with the software OOMMF 1.2A3,[52] the material parameters for Permalloy are chosen: saturation magnetization $M_s=860\times10^3$ A/m, exchange stiffness $A=13\times10^{-12}$ J/m, anisotropy constant $K_1=0$, and damping coefficient $\alpha=0.5$. The circular dot has a diameter of 0.8 μm and a thickness of 60 nm, and it is discretized into quadratic cells of 10 nm side length.

In Fig. 7 the ascending branch of the hysteresis loop and selected magnetization profiles are depicted. As it is typical for an ideal vortex configuration, the y component of the magnetization is zero. Coming from negative saturation field (1) to point (2) the core of the vortex develops abruptly at the nucleation field $H_N=-50$ Oe. In the remanent state (3) the core has moved into the center of the circular dot. Increasing further the field leads to a movement of the core to the upper edge (4), and again the core vanishes abruptly at the extinction field $H_e=90$ Oe [step in the hysteresis loop between (4) and (5)]. Figure 8 shows the real and imaginary parts of the magnetic form factor f_{hk}^m, either $h=1,2,3$ or $k=1,2,3$, for the x and y components of the magnetization; only the ascending branch is depicted. Since the circular dots are set on a square lattice with periodicities $d_x=d_y=1.6$ μm the diffraction pattern is a two-dimensional one. For each magnetization component the form factors are obtained from the hth diffraction order lying in the plane of incidence as well as from the kth diffraction order perpendicular to the plane of incidence. As can be seen in these plots the magnetization component as well as the specific diffraction order has a strong influence on the behavior of the real and imaginary

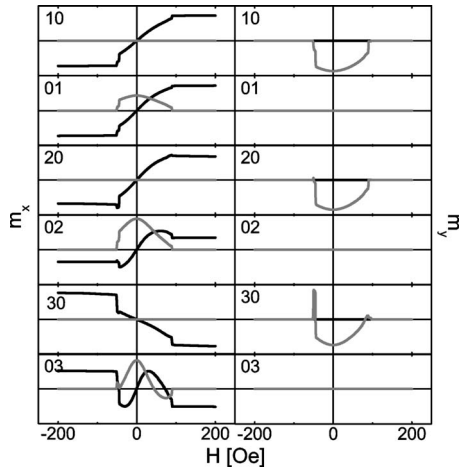

FIG. 8. Real (black lines) and imaginary (gray lines) form factors for the x (left panel) and the y component (right panel) calculated for the periodicities $d_x=d_y=1.6$ μm.

parts of f_{hk}^m. The plots for m_x obtained at the diffraction spots h are similar in shape: the real part of all form factors is similar to the hysteresis curve in Fig. 7, and the imaginary part is zero. At the diffraction spots k the shape of the form factors for m_x changes with the diffraction order. The real part and the imaginary part are unequal to zero. The plots show for higher diffraction orders more oscillations in the field region where the vortex moves through the dot. Either the real or the imaginary form factor passes through the origin. This is true for all cases where the periodicity is an integer multiple of the diameter.

One central and challenging task of Bragg-MOKE is the determination of the chirality of the vortices inside of the magnetic dots (here, chirality is used in the meaning of the rotational sense of the vortex). In fact, the chirality can be determined from the sign of the real and imaginary form factors of kth diffraction order at positions perpendicular to the scattering plane. This behavior is displayed in Fig. 9. The left panel shows the form factor for the case of counterclockwise vortex chirality, and the middle panel for the clockwise chirality. The sign of the real part of the form factor is preserved, and the sign of the imaginary part changes. The change in chirality corresponds to a change in sign of the position component y and magnetization compo-

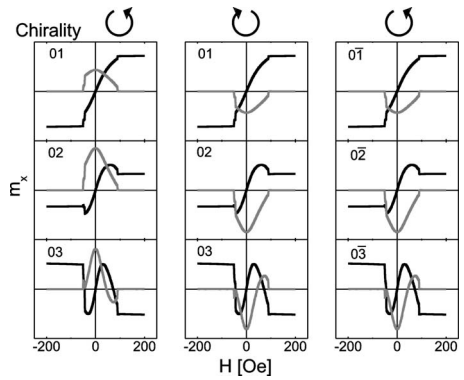

FIG. 9. Real (black lines) and imaginary (gray lines) form factors for counterclockwise and clockwise vortex chiralities obtained at kth diffraction orders ($h=0$). Note that the chirality follows from the out-of-plane reflections.

nent m_y; $y \rightarrow -y$, $m_y \rightarrow -m_y$. This is easy to understand because the form factors are odd functions concerning the magnetization. Concerning the phase factor the real part corresponds to an even function and the imaginary one to an odd function. Assuming that the factor A_l in Eq. (15) does not change sign, the hysteresis curve will behave different for different vortex chiralities. For the sake of completeness the right panel in Fig. 9 shows the form factor for the counterclockwise chirality at the negative diffraction order k. The relative sign of the imaginary parts also depends on the sign of the diffraction order.

In Fig. 8 the form factors of the m_y component are also depicted. The form factors of all diffraction orders k are zero as the y component of the hysteresis curves is zero. In the diffraction order h only the imaginary part is unequal to zero. For $k=3$ a sharp peak is observed at the field where the vortex core develops (point 2 in Fig. 7). This behavior can be explained with the nature of the form factor. The magnetic form factor corresponds to a Fourier transformation of the magnetization configuration. Thus, it becomes more sensitive to the domain configuration at the sample edges with higher order h,k.

Bragg-MOKE hysteresis curves of circular islands with vortex state are discussed in the work of Grimsditch *et al.*[46] using the Kerr effect in transverse geometry and—in more detail—in the work of Lee *et al.*[53] using the longitudinal Kerr geometry. Lee *et al.* investigated the Bragg-MOKE signal of Permalloy dots (diameter of 0.8 μm) at the diffraction spots $(0k)$ for both magnetization components m_x and m_y and at the diffraction spots $(h0)$ for the magnetization component m_x. The measurements reflect the behavior of the Bragg-MOKE curves discussed in this paper very well. For a detailed description the reader is referred to the abovementioned reference.

Finally, in an array of dots, which is one prerequisite for Bragg-MOKE experiments, the vortex state of the magnetization will not show the same chirality in all dots. In principle, in an array of ideal circular dots the vortex chirality should be 50% clockwise and 50% counterclockwise during the remagnetization process. In such a case the Bragg-MOKE signal will not contain any information about the chirality because this measurement technique integrates over the magnetization of all dots illuminated by the laser beam. But in reality, the fabrication of ideal circular dots is difficult. Real dots have more or less asymmetries influencing a defined chirality of the vortex state. This will lead to the situation that one chirality dominates and a well defined Bragg-MOKE signal can be measured. If a strong asymmetry is introduced in the dots (e.g., a flat edge[54]) the magnetization will show the same chirality in all dots during the remagnetization process.

B. Edge domains in ferromagnetic stripes

In the next example the remagnetization process of a ferromagnetic stripe orientated with the hard axis magnetization parallel to the field is discussed. It is assumed that the stripe is infinitely long in the y direction. In the micromagnetic simulation the stripe is required to have a finite length, which is compensated for by assuming a high aspect ratio. For the simulation the material parameters of Fe are chosen: saturation magnetization $M_s=1700\times10^3$ A/m, exchange stiffness $A=21\times10^{-12}$ J/m, anisotropy constant $K_1=48\times10^3$ J/m^3, and damping coefficient $\alpha=0.5$. The stripe has a length of 200 μm, a width of 2 μm, and a thickness of 50 nm, and it is discretized into quadratic cells of 100 nm side length.

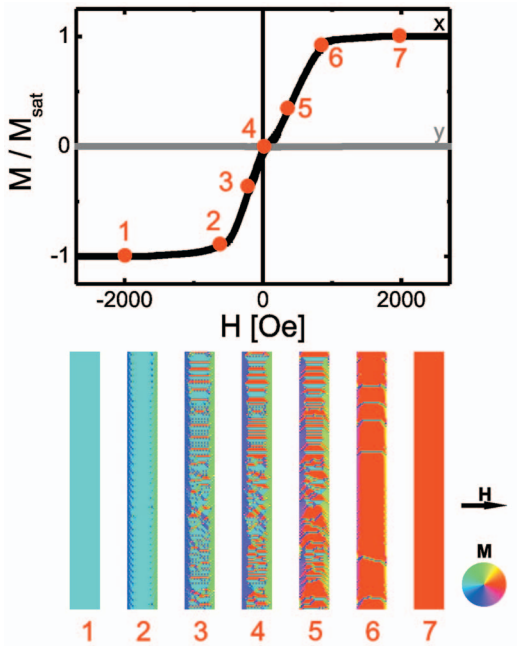

FIG. 10. (Color) Ascending branch of the hysteresis loop for the x (black line) and the y component (gray line) of the magnetization, and some selected calculated magnetization profiles.

Figure 10 shows the ascending branch of the zeroth-order hysteresis loops for both the x and the y component of the magnetization. Like for the vortex the y component of the magnetization is not affected during the reversal process. On the average the magnetization component m_y cancels out. The x component shows a typical hard axis behavior. Coming from negative saturation field (1) first domains develop at the edges of the stripe (2). In the magnetization profile at point (3) edge domains with the magnetization directions along the stripe are formed, whereas the magnetization points into opposite direction at the opposite edges. The area between the edges breaks up into domains with a net magnetization parallel to the field. In Fig. 11 the real and imaginary form factors of the x component for $h=1-6$ are depicted for two different periodicities $d_x=4$ and 5 μm. As the diffraction pattern from the stripe array is one dimensional, only the form factors of the magnetization component m_x are taken into account, which are lying in the scattering plane. In the first case with $d_x=4$ μm the shape of the form factors repeats in the different orders h, one of the form factors, either the real or imaginary part is always nearly zero. At the odd orders the form factor curves equal the hysteresis curve, at the even orders the form factor curves show an N shape. The maximum occurs in the field region where the domains between the edges develop and the minimum in the field region where they vanish. In the second case with $d_x=5$ μm both the real and the imaginary form factors

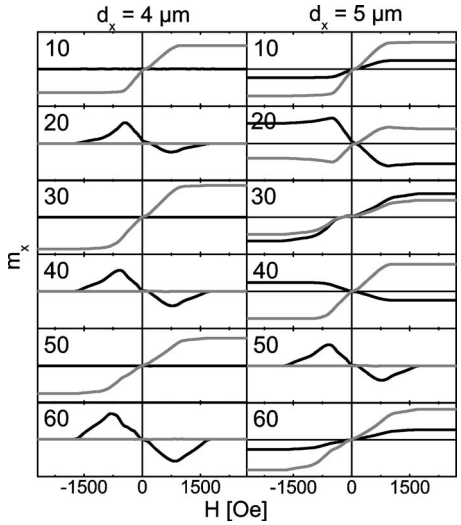

FIG. 11. Real (black lines) and imaginary (gray lines) form factors for the x component calculated for two different periodicities d_x as indicated in the figure (left panel: d_x=4 μm, right panel: d_x=5 μm) and for different orders $h0$ of diffraction.

contribute to the Bragg-MOKE signal. In principle the form factors behave like the hard axis hysteresis loop. The form factor curves at h=2 show overshoots at the field values where the N-shape form factor curve of h=5 has its maximum and minimum which are at the same field values as for d_x=4 μm. Drastic changes of the form factor and development of an N shape occur whenever the relation $hd=zw$ is fulfilled with h the order of the form factor, d the periodicity, w the width of the stripe width, and z an integer number. This behavior agrees with the observation and measurements discussed in Ref. 17. The authors investigated the Bragg-MOKE signal at the (h0) diffraction spots of a two-dimensional periodic array (periodicity of 6 μm in one direction and 42 μm in the orthogonal direction) of two separated polycrystalline Fe rectangles, both being 30 μm long, one having a width of 0.9 μm and the other one of 1.9 μm. An example of the results is given in Fig. 12. It shows the measured and calculated Bragg-MOKE at the diffraction spots (30). The N shape of the hysteresis curve

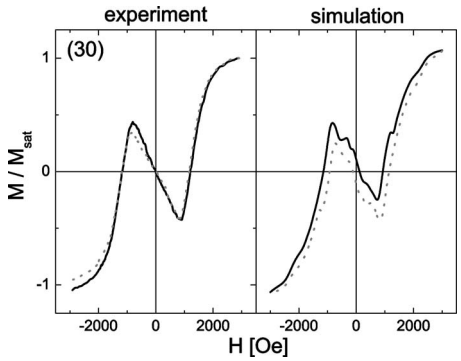

FIG. 12. Measured (left) and calculated (right) Bragg-MOKE hysteresis curves of rectangular Fe islands described in Ref. 17. Only the diffraction order (30) is shown as an example. The hysteresis curves have been normalized to saturation magnetization. Solid (dashed) line represents increasing (decreasing) magnetic field.

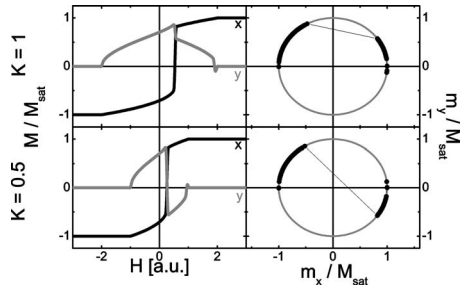

FIG. 13. The left plots show the ascending branch of the hysteresis loops both for the x (black line) and and the y component (gray line) of the magnetization. The right plots show the y component of the magnetization as a function of the x component; thus, the plots describe the path of the magnetization vector. The calculations are performed for two different anisotropy values, K=1 (top panel) and K=0.5 (bottom panel). For further explanations the reader is referred to the text.

is clearly visible. In this case the relation $hd=zw$ with h=3, d=6 μm, and w=4.5 μm is fullfilled with z=4.

C. Coherent rotation

In the third example a coherent rotation of the magnetization is considered. The easiest way to investigate this process is the use of a Stoner-Wohlfarth model.[55] The minimization of the following energy term leads to the magnetization components m_x and m_y for a given applied field H:

$$E = -M_{\mathrm{sat}} H \cos\chi + \tfrac{1}{4} K \sin^2[2(\chi + 45^\circ)], \tag{33}$$

where χ is the angle between the x axis and the magnetization vector, therefore $m_x=\cos\chi$ and $m_y=\sin\chi$. The energy term describes a sample with a fourfold anisotropy where the hard axis direction is parallel to the x axis. The calculation has been performed with reduced anisotropies K=1 and K=0.5 and saturation magnetization M_{sat}=1 in the field region between $H=-4$ and 4.

The ascending branches of typical hysteresis loops of the x and y components for the coherent rotation process are depicted in Fig. 13. The step in the hysteresis indicates the sudden change in the direction of the magnetization vector which can be easily seen in the plots of the magnetization path (m_y-m_x plots on the right side of Fig. 13). Assuming that the coherent rotation process takes place in squares with a side length of w=1 μm arranged in a square array with periodicities of $d_x=d_y$=2 μm or d_x=2.5 μm and d_y=3 μm different behaviors in the real and imaginary form factors are observed (see Figs. 14 and 15). For the case that the periodicity is equal in the x and y directions (Fig. 14), either the real or the imaginary form factor is zero. At odd diffraction orders the real part is zero, at even diffraction orders the imaginary part of the magnetic form factor is zero. The form factors of m_x obtained from the diffracted beams of order h and k equal to the hysteresis curve of m_x measured at the specular beam in Fig. 13. The form factors of m_y behave in the same manner concerning m_y in the hysteresis curve. Thus, a remagnetization process via coherent rotation is represented by order-independent hysteresis loops due to the nature of the Fourier transformation.

The change in the anisotropy constant K affects on the one hand the coercive field strength and on the other hand

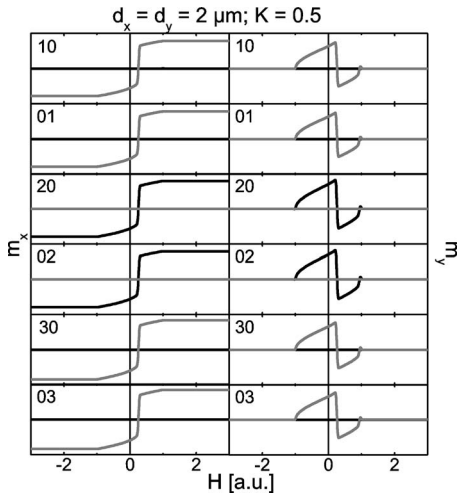

FIG. 14. Real (black lines) and imaginary (gray lines) form factors for the x (left panel) and the y component (right panel) calculated for the periodicities $d_x=d_y=2$ μm and the anisotropy constants $K=0.5$.

the shape of the hysteresis curve of the y component. The reason is visible in the m_y-m_x plots in Fig. 13: in the first case ($K=1$) the magnetization vector rotates only in the upper part of the plot, i.e., the y component of the magnetization does not change sign. In the second case ($K=0.5$) the magnetization vector switches more around and changes the sign in the y component during the reversal process.

For the case of different periodicities d_x and d_y (Fig. 15) both form factors contribute. The shape of the form factor curves equals for all orders the hysteresis curves in Fig. 13. This behavior agrees with the observations and measurements discussed by Remhof *et al.* in Ref. 56. The authors investigated hysteresis curves at diffraction spots $h0$ of an array of polycrystalline, rectangular Permalloy islands with a lateral size of 0.3×3 μm^2 (thickness of 25 nm) setting in a square grid with a periodicity of 5 μm. As the Permalloy islands were prepared to be single domain particles the expected coherent rotation of the magnetic moments toward the easy axis given by the shape anisotropy of the islands, i.e.,

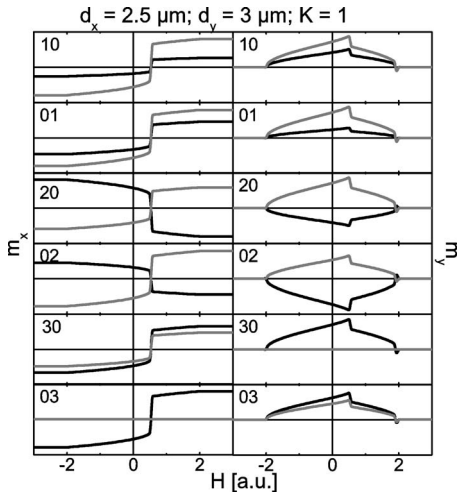

FIG. 15. Real (black lines) and imaginary (gray lines) form factors for the x (left panel) and the y component (right panel) calculated for the periodicities $d_x=2.5$ μm and $d_y=3$ μm and the anisotropy constants $K=1$.

parallel to the long axis of the islands, is manifested in order-independent hysteresis loops.

D. Concluding remarks

Depending on the process which dominates the remagnetization, the form factors and thus the diffraction hysteresis loops can adopt different shapes. But there are general properties to be noted.

- In the case of coherent rotation the form of the diffraction hysteresis loops of order $h\neq0$, $k\neq0$, equals the hysteresis loop measured at the specular spot $h=k=0$.
- The form factor curves show steps and overshoots if the domain configuration changes drastically, e.g., if new domains appear or the magnetization directions change abruptly.
- The periodicity of the lateral structure has an effect on the interplay between the real and the imaginary form factor.
- In the example with the ferromagnetic stripe array the diffraction hysteresis loop shows an amplified N-shape behavior if the product of the stripe width w and the order h is a multiple integer of the periodicity d: $zd=hw$.

VI. SECOND-ORDER MOKE

As discussed in the previous sections, longitudinal Kerr magnetometry is an easy method for the characterization of the magnetization reversal in thin films. One of the drawbacks of this method is the occurrence of asymmetries in the Kerr hysteresis loops,[57–59] in contrast to transverse Kerr magnetometry. These asymmetries derive mainly from higher order contributions in the Kerr rotation which complicate an easy interpretation. On the other hand the optical setup can also play a role. The asymmetries are caused by second-order terms of the dielectric tensor ϵ.[60] The second-order terms describe the inherent dielectric properties of the magnetic film, from which follows that they are quadratic in the magnetization. The microscopic source of the asymmetry in the magneto-optic response is a second-order term in the spin-orbit interaction. The asymmetry is in many cases observed in magnetic films with in-plane anisotropy.[26]

Nevertheless, the quantitative determination of the so-called Voigt-effect contribution to the longitudinal Kerr effect can easily be done by measuring the longitudinal Kerr signal of a saturated sample with a rotating magnetic field.[61] The Voigt-effect contribution is also called quadratic MOKE[62] or second-order MOKE contribution.[26] It becomes the only important term in case of normal incidence.

In experiments a saturation field should be applied which is considerably stronger than the anisotropy field strength H_K. If the applied field is now rotated, the direction of the magnetization of the sample points, at least in the limit of an infinite magnetic field, in the direction of the field. Therefore a coherent magnetization reversal is realized (like the Stoner-Wohlfarth behavior), avoiding all problems caused by hysteresis effects. The Kerr signal θ_K is recorded as a function of the field rotation β. Here, the zero point of the rotation corresponds to the longitudinal axis of the experimental setup. In Ref. 26 the authors included second-order terms in the

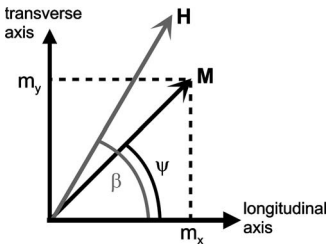

FIG. 16. Definition of the angles β and ψ with respect to the longitudinal and vertical axes.

dielectric tensor of a cubic crystal resulting in $m_x m_y$ terms for the second-order effects and longitudinal geometry. In Ref. 59 fits to MOKE data in the longitudinal geometry prove that the Kerr signal can be described effectively by

$$\theta_K = \theta_0 + q \cos \psi + b \cos \psi \sin \psi + c \sin^2 \psi, \tag{34}$$

where ψ is the angle between the magnetization vector and the longitudinal axis (see Fig. 16), q, b, and c are parameters which depend on the optic geometry (e.g., polarization angle, incident angle) and the dielectric tensor of the material,[27,58] and θ_0 is the magnetization independent magneto-optical activity of the sample. Equation (34) is a general description for second-order contribution. In the case of a very large rotating field the angle ψ is identical to the angle β which describes the rotation of the field. Then,

$$m_x = \cos \beta, \quad m_y = \sin \beta. \tag{35}$$

Performing vector MOKE, $\sin \psi$ and $\cos \psi$ have different meanings depending on what component of the magnetization vector is under investigation. From the sketches in Figs. 4 and 16 it can be seen that for the x component $\theta_K = \theta_x$ and the terms are identified to

$$m_x = \cos \psi, \quad m_y = \sin \psi \tag{36}$$

and for the y component $\theta_K = \theta_y$,

$$m_x = \sin \psi, \quad m_y = \cos \psi. \tag{37}$$

If second-order effects influence the shape of Bragg-MOKE curves, calculated and measured ones can be compared using Eq. (34). With the additional terms the shape of the measured hysteresis can be reproduced from the micromagnetic simulations by taking the results for m_x and m_y from the micromagnetic simulations and fitting them to the measured hysteresis data. An example using this method can be found in Ref. 15.

Now we return to the determination of second-order effects. From the measured $\theta_K(\beta)$ values a FFT can be performed to determine amplitude and phase of the $(n\beta)$ terms. From the result of the FFT the contributions of the linear and second-order effect to the measured Kerr signal can be distinguished.

The Kerr magnetometry with the rotating magnetic field of constant amplitude can also be used to determine the anisotropy field strength and their symmetry axis distribution. This technique is called the ROTMOKE method,[63] examples can be found in Refs. 64–67. It is also used in the transverse Kerr geometry and called magneto-optical torque technique.[68–70]

VII. SUMMARY

Lateral micro-or nanosized magnetic structures work as diffraction gratings: illuminating the structure with the laser beam of a MOKE setup leads to an interference pattern. The Kerr signals measured at the diffraction spots gain information about the domain configuration in the elements (Bragg-MOKE). Furthermore, the MOKE technique can be used to obtain vectorial information of the magnetization process (vector MOKE) both at the specular spot and the higher order diffraction spots. The vector MOKE technique is an extension of the standard longitudinal Kerr effect. A field applied in the transverse geometry, i.e., perpendicular to the scattering plane, allows the determination of the two orthogonal components of the magnetization vector in two successive measurements at the specular spot. At the higher order diffraction spots the vector MOKE signal contains information of the magnetic form factors of the two orthogonal magnetization components. Both techniques were described in detail in this paper and several examples were given. Vector and Bragg-MOKEs allow a deeper insight in the remagnetization process of micro- and nanostructured ferromagnetic elements. The measurement of a standard hysteresis loop in the usually used MOKE technique, i.e., a hysteresis loop obtained in longitudinal Kerr geometry at the specular spot, contains only the information on the m_x component of the magnetization vector integrated over the region illuminated by the laser beam. With this information it is not possible to characterize the remagnetization process in detail, e.g., one could not distinguish between domain formation and coherent rotation of the net magnetization vector. Differences in the remagnetization process are visible in the Bragg-MOKE signal of the m_x and m_y components of the magnetization vector because the Bragg-MOKE technique is sensitive to the inner domain configuration in the lateral structure, and standard Kerr hysteresis loops only measure the net magnetization of the m_x component.

For the interpretation of the measured data it is necessary to perform micromagnetic simulations using, for example, the public domain software of the object orientated micromagnetic framework (OOMMF 1.2A3) project at ITL/NIST. The micromagnetic simulation yields magnetization profiles of a lateral structure for different field values and, thus, information on the domain configuration. With the magnetization profiles it is possible to calculate the magnetic form factor and to reconstruct the measured Bragg-MOKE hysteresis loops. If the calculated hysteresis loops agree with the measured Bragg-MOKE ones both for the m_x component and the m_y component of the magnetization vector, the results of the micromagnetic simulation are reliable and reflect the remagnetization process of the lateral structure.

MOKE is an integrating technique, i.e., the average net magnetization of the illuminated area is measured. Assuming that the single elements of a lateral structure do not influence each other by stray field coupling, the Kerr signal contains the information on an average remagnetization process in the elements. In this case it is sufficient to take one single element into account for the micromagnetic simulation. For a lateral structure where the single elements communicate by

stray field coupling, a larger section with an adequate number of elements has to be considered in the micromagnetic simulation. Depending on the size this will limit the accuracy of the simulation because of restricted computational power.

There are many other examples which underline the user friendly and successful aspects of the Kerr magnetometry: ac-MOKE allows to measure the ac susceptibility of ferromagnetic thin films,[71] the transverse bias inverse initial susceptibility and torque method allows the simultaneous determination of the torque and the initial inverse susceptibility resulting in the determination of the magnetic anisotropy energy,[72] or one can measure the magnetic anisotropy with the modulated field magneto-optical anisometry technique,[73] with Kerr microscopy it is possible to image domain pattern in real space.[74]

ACKNOWLEDGMENTS

This work was supported by SFB 491 of the Deutsche Forschungsgemeinschaft: "Magnetic Heterostructures: Spin Structures and Spin Transport," which is gratefully acknowledged.

[1] S. Tehrani, J. Slaughter, M. DeHerrera, B. Engel, N. Rizzo, J. Salter, M. Durlam, R. Dave, J. Janesky, B. Butcher, K. Smith, and G. Grynkewich, Proc. IEEE **91**, 703 (2003).
[2] J. I. Martín, J. Nogués, K. Liu, J. L. Vicent, and I. K. Schuller, J. Magn. Magn. Mater. **256**, 449 (2003).
[3] G. Dumpich, T. P. Krome, and B. Hausmanns, J. Magn. Magn. Mater. **248**, 241 (2002).
[4] B. Hausmanns, T. P. Krome, and G. Dumpich, J. Appl. Phys. **93**, 8095 (2003).
[5] W. C. Uhlig and J. Shi, Appl. Phys. Lett. **84**, 759 (2003).
[6] A. A. Fraerman, S. A. Gusev, L. A. Mazo, I. M. Nefedov, I. R. Karetnikova, Yu. N. Nozdrin, M. V. Sapozhnikov, I. A. Shereshevskii, and L. V. Sukhodoev, Phys. Rev. B **65**, 064424 (2002).
[7] T. Uhlig and J. Zweck, Phys. Rev. Lett. **92**, 047203 (2004).
[8] A. Kuksov, C. Schneider, A. Oelsner, A. Krasyuk, D. Neeb, G. Schönhense, C. D. Nadaï, and N. Brookes, J. Appl. Phys. **95**, 6530 (2004).
[9] T. Eimüller, M. Scholz, P. Guttmann, P. Fischer, M. Köhler, G. Bayreuther, G. Schmahl, and G. Schütz, J. Appl. Phys. **89**, 7163 (2001).
[10] M. Natali, I. L. Prejbeanu, A. Lebib, L. D. Buda, K. Ounadjela, and Y. Chen, Phys. Rev. Lett. **88**, 157203 (2002).
[11] J. McCord, R. Schäfer, K. Theis-Bröhl, H. Zabel, J. Schmalhorst, and H. Brückl, J. Appl. Phys. **97**, 10K102 (2005).
[12] K. Theis-Bröhl, M. Wolff, A. Westphalen, H. Zabel, J. McCord, V. Häoink, J. Schmalhorst, T. Weis, D. Engel, A. Ehresmann, U. Rücker, and B. P. Toperverg, Phys. Rev. B **73**, 174408 (2006).
[13] P. Cowburn, D. K. Koltsov, A. O. Adeyeye, and M. E. Welland, Appl. Phys. Lett. **73**, 3947 (1998).
[14] M. Grimsditch and P. Vavassori, J. Phys.: Condens. Matter **16**, R275 (2004).
[15] A. Westphalen, A. Schumann, A. Remhof, H. Zabel, T. Last, and U. Kunze, Phys. Rev. B **74**, 104417 (2006).
[16] T. Schmitte, K. Theis-Bröhl, V. Leiner, H. Zabel, S. Kirsch, and A. Carl, J. Phys.: Condens. Matter **14**, 7525 (2002).
[17] A. Westphalen, K. Theis-Bröhl, H. Zabel, K. Rott, and H. Brückl, J. Magn. Magn. Mater. **302**, 181 (2006).
[18] A. Westphalen, T. Schmitte, K. Westerholt, and H. Zabel, J. Appl. Phys. **97**, 073909 (2005).
[19] C.-Y. You and S.-C. Shin, Appl. Phys. Lett. **69**, 1315 (1996).
[20] T. Zeidler, F. Schreiber, H. Zabel, W. Donner, and N. Metoki, Phys. Rev. B **53**, 3256 (1996).
[21] R. C. Jones, J. Opt. Soc. Am. **31**, 488 (1941).
[22] T. Schmitte, Ph.D. thesis, Ruhr University Bochum, Germany, 2003.
[23] C. Daboo, J. Bland, R. Hicken, A. Ives, M. Baird, and M. Walker, Phys. Rev. B **47**, 11852 (1993).
[24] H. Ohldag, N. B. Weber, F. U. Hillebrecht, and E. Kisker, J. Appl. Phys. **91**, 2228 (2002).
[25] P. Vavassori, Appl. Phys. Lett. **77**, 1605 (2000).
[26] R. M. Osgood III, S. D. Bader, B. M. Clemens, R. L. White, and H. Matsuyama, J. Magn. Magn. Mater. **182**, 297 (1998).
[27] J. M. Florczak and E. D. Dahlberg, J. Appl. Phys. **67**, 7520 (1990).
[28] O. Geoffroy, D. Givord, Y. Otani, B. Pannetier, A. D. Santos, and M. Schlenker, J. Magn. Magn. Mater. **121**, 516 (1993).
[29] J. Kranz and C. Schrödter, Appl. Phys. A: Solids Surf. **31**, 59 (1983).
[30] D. van Labeke, A. Vial, V. A. Novosad, Y. Souche, M. Schlenker, and A. D. D. Santos, Opt. Commun. **124**, 519 (1996).
[31] A. Vial and D. van Labeke, Opt. Commun. **153**, 125 (1998).
[32] A. Bengoechea, G. Armelles, J. L. Costa-Krämer, and J. Anguita, Phys. Rev. B **73**, 205402 (2006).
[33] N. Bardou, B. Bartenlian, F. Rousseaux, D. Decanini, F. Carcenac, C. Chappert, P. Veillet, P. Beauvillain, R. Mégy, Y. Suzuki, and J. Ferré, J. Magn. Magn. Mater. **148**, 293 (1995).
[34] Y. Souche, M. Schlenker, and A. D. D. Santos, J. Magn. Magn. Mater. **140–144**, 2179 (1995).
[35] V. Eremenko, V. Novosad, V. Pishko, O. Geoffroy, Y. Souche, and B. Pannetier, JETP Lett. **66**, 494 (1997).
[36] S. Gadetsky, I. Syrgabaev, J. K. Erwin, M. Mansuripur, T. Suzuki, and M. Ruane, J. Opt. Soc. Am. A **13**, 314 (1996).
[37] P. Vavassori, V. Metlushko, R. M. Osgood III, M. Grimsditch, U. Welp, G. Crabtree, W. Fan, S. R. J. Brueck, B. Ilic, and P. J. Hesketh, Phys. Rev. B **59**, 6337 (1999).
[38] I. Guedes, M. Grimsditch, V. Methlushko, P. Vavassori, R. Camley, B. Ilic, P. Neuzil, and R. Kumar, Phys. Rev. B **67**, 024428 (2003).
[39] J. L. Costa-Krämer, C. Guerrero, S. Melle, P. García-Mochales, and F. Briones, Nanotechnology **14**, 239 (2003).
[40] Y. Suzuki, C. Chappert, P. Bruno, and P. Veillet, J. Magn. Magn. Mater. **165**, 516 (1997).
[41] L. Wenzel, A. Hubert, and V. Kamberský, J. Magn. Magn. Mater. **175**, 205 (1997).
[42] T. Schmitte, T. Schemberg, K. Westerholt, H. Zabel, K. Schädler, and U. Kunze, J. Appl. Phys. **87**, 5630 (2000).
[43] A. Westphalen, A. Schumann, A. Remhof, H. Zabel, T. Last, and U. Kunze, Superlattices Microstruct. **41**, 98 (2007).
[44] I. Guedes, N. J. Zaluzec, M. Grimsditch, V. Metlushko, P. Vavassori, B. Ilic, P. Neuzil, and R. Kumar, Phys. Rev. B **62**, 11719 (2000).
[45] I. Guedes, M. Grimsditch, V. Metlushko, P. Vavassori, R. Camley, B. Ilic, P. Neuzil, and R. Kumar, Phys. Rev. B **66**, 014434 (2002).
[46] M. Grimsditch, P. Vavassori, V. Novosad, V. Metlushko, H. Shima, Y. Otani, and K. Fukamichi, Phys. Rev. B **65**, 172419 (2002).
[47] T. Schmitte, O. Schwöbken, S. Goek, K. Westerholt, and H. Zabel, J. Magn. Magn. Mater. **240**, 24 (2002).
[48] T. Schmitte, K. Westerholt, and H. Zabel, J. Appl. Phys. **92**, 4524 (2002).
[49] J. L. Costa-Krämer, R. Alvarez-Sánchez, A. Bengoechea, F. Torres, P. García-Mochales, and F. Briones, Phys. Rev. B **71**, 104420 (2005).
[50] R. M. A. Azzam and N. M. Bashara, Phys. Rev. B **5**, 4721 (1972).
[51] A. K. Zvezdin and V. A. Kotov, *Modern Magnetooptics and Magnetooptical Materials* (IOP, Bristol, 1997).
[52] M. J. Donahue and D. G. Porter, Interagency Report No. NISTIR 6376 (National Institute of Standards and Technology, Gaithersburg, MD, 1999).
[53] M.-S. Lee, A. Westphalen, A. Remhof, A. Schumann, and H. Zabel, "Detecting the chirality distribution of magnetic vortices in Py nanodots by longitudinal Bragg MOKE," Europhys. Lett. (submitted).
[54] M. Schneider, H. Hoffmann, and J. Zweck, Appl. Phys. Lett. **79**, 3113 (2001).
[55] E. C. Stoner and E. P. Wohlfarth, Philos. Trans. R. Soc. London, Ser. A **240**, 599 (1948).
[56] A. Remhof, C. Bircan, A. Westphalen, J. Grabis, A. Nefedov, and H. Zabel, Superlattices Microstruct. **37**, 353 (2005).
[57] Q.-M. Zhong, A. S. Arrott, B. Heinrich, and Z. Celinski, J. Appl. Phys. **67**, 4448 (1990).
[58] R. M. Osgood III, B. M. Clemens, and R. L. White, Phys. Rev. B **55**, 8990 (1997).
[59] S. Yan, R. Schreiber, P. Grünberg, and R. Schäfer, J. Magn. Magn. Mater. **210**, 309 (2000).
[60] W. Wettling, J. Magn. Magn. Mater. **3**, 147 (1976).
[61] R. Mattheis and G. Quednau, Phys. Status Solidi A **172**, 143 (1999).
[62] K. Postava, H. Jaffres, A. Schuhl, F. Nguyen Van Dau, M. Goiran, and A. R. Fert, J. Magn. Magn. Mater. **172**, 199 (1997).
[63] R. Mattheis and G. Quednau, J. Magn. Magn. Mater. **205**, 143 (1999).

[64] K.-U. Barholz and R. Mattheis, J. Appl. Phys. **91**, 7224 (2002).
[65] O. de Haas, R. Schäfer, L. Schultz, K.-U. Barholz, and R. Mattheis, J. Magn. Magn. Mater. **260**, 380 (2003).
[66] Z. Tian, C. S. Tian, L. F. Yin, D. Wu, G. S. Dong, X. F. Jin, and Z. Q. Qiu, Phys. Rev. B **70**, 012301 (2004).
[67] C. S. Tian, D. Qian, D. Wu, R. H. He, Y. Z. Wu, W. X. Tang, L. F. Yin, Y. S. Shi, G. S. Dong, X. F. Jin, X. M. Jiang, F. Q. Liu, H. J. Qian, K. Sun, L. M. Wang, G. Rossi, Z. Q. Qiu, and J. Shi, Phys. Rev. Lett. **94**, 137210 (2005).
[68] G. Armelles, J. L. Costa-Krämer, J. Martin, J. V. Anguita, and J. L. Vicent, Appl. Phys. Lett. **77**, 2039 (2000).
[69] D. Jaque, J. I. Martín, G. Armelles, J. L. Costa-Krämer, F. Briones, and J. L. Vicent, J. Appl. Phys. **91**, 382 (2002).
[70] P. Gracía-Mochales, J. L. Costa-Krämer, G. Armelles, F. Briones, D. Jaque, J. I. Martín, and J. L. Vicent, Appl. Phys. Lett. **81**, 3206 (2002).
[71] A. Berger, S. Knappmann, and H. P. Oepen, J. Appl. Phys. **75**, 5598 (1994).
[72] D. Berling, S. Zabrocki, R. Stephan, G. Garreau, J. L. Bubendorff, A. Mehdaoui, D. Bolmont, P. Wetzel, C. Pirri, and G. Gewinner, J. Magn. Magn. Mater. **297**, 118 (2006).
[73] R. P. Cowburn, A. Ercole, S. J. Gray, and J. A. C. Bland, J. Appl. Phys. **81**, 6879 (1997).
[74] E. Feldtkeller and K. U. Stein, Z. Angew. Phys. **23**, 100 (1967).